



Site-specific chemical doping reveals electron atmospheres at the surfaces of organic semiconductor crystals

Tao He[⊕]^{1,2}, Matthias Stolte³, Yan Wang[⊕]^{1,4}, Rebecca Renner³, P. Paul Ruden⁵, Frank Würthner[⊕]³ and C. Daniel Frisbie[⊕]¹

Chemical doping controls the electronic properties of organic semiconductors, but so far, doping protocols and mechanisms are less developed than in conventional semiconductors. Here we describe a unique, site-specific, n-type surface doping mechanism for single crystals of two benchmark organic semiconductors that produces dramatic improvement in electron transport and provides unprecedented evidence for doping-induced space charge. The surface doping chemistry specifically targets crystallographic step edges, which are known electron traps, simultaneously passivating the traps and releasing itinerant electrons. The effect on electron transport is profound: field-effect electron mobility increases by as much as a factor of ten, and its temperature-dependent behaviour switches from thermally activated to band-like. Our findings suggest new site-specific strategies to dope organic semiconductors that differ from the conventional redox chemistry of randomly distributed substitutional impurities. Critically, they also verify the presence of doping-induced electron atmospheres, confirming long-standing expectations for organic systems from conventional solid-state theory.

hemical doping plays a central role in the science and applications of organic semiconductor materials¹⁻⁶. Decades ago, the discovery that crystals and films of pi-conjugated molecules could be made highly conducting, and even metallic, by chemical doping (for example, conducting polymers) sparked world-wide interest in these materials and marked a critical turning point in the field of organic electronics⁷⁻¹³. Today, p- and n-type doping of organic semiconductor films is used industrially to lower the operating voltages of organic light-emitting diode displays^{1,14,15}. Still, many structural and electronic aspects of chemical doping in organic semiconductors remain poorly understood, particularly for crystalline or polycrystalline systems where strong anisotropic intermolecular interactions, crystalline defects and microstructure can be decisive in determining the doping mechanism and ionization efficiency¹⁶⁻²¹.

Here we report two discoveries related to chemical doping of organic semiconductors. First, we have found that crystallographic step edges on the surfaces of specific organic semiconductor crystals can be selectively n-doped. This site-specific doping eliminates shallow electron traps at the step edges and results in dramatic recovery of band-like transport properties for crystals that, before doping, had low field-effect electron mobilities and strongly activated (trap-limited) transport. This intriguing result indicates site-specific doping may be a productive new strategy for improved material performance in organic electronics. Second, we have discovered that doping-induced electron atmospheres along the step edges can be visualized by scanning Kelvin probe microscopy (SKPM). The SKPM images represent direct detection of space charge associated with chemical doping in an organic semiconductor and provide critical verification of microscopic doping effects

in organic systems that match expectations from classical inorganic semiconductor physics.

Our study focuses on crystals of Cl₂-NDI (refs. ^{22,23}) (space group $P\bar{1}$) and PDIF-CN₂ (refs. ^{24,25}) (space group $P\bar{1}$), respectively, Fig. 1, well-known semiconducting materials that exhibit outstanding n-channel performance in field-effect transistors (FETs). Exposure of the (001) surfaces of both crystals to an N-silane vapour ((3-(2-aminoethylamino)propyl)trimethoxysilane, 1a) results in n-type doping that is evident in FET measurements, as described below. Our motivation to use this amine as a dopant was based in part on the known redox reactivity of Cl₂-NDI and PDIF-CN₂ with amines, and in part on trial-and-error experiments with a variety of different amines (Supplementary Figs. 1-3)^{26–30}. Spectroelectrochemistry and ultraviolet-visible light (UV-vis) titration studies confirm that the N-silane in Fig. 1a reduces Cl₂-NDI and PDIF-CN₂ in solution (Supplementary Figs. 4 and 5), and we hypothesized that spontaneous electron transfer from the amines to the crystals could produce n-type surface doping.

To test this hypothesis, we grew lath-like crystals of Cl₂-NDI and PDIF-CN₂ with thicknesses ranging from 1 to 50 µm by physical vapour transport and laminated the crystals onto Au-coated polydimethylsiloxane (PDMS) stamps to make four-terminal 'air-gap' FETs (Fig. 1a)^{25,31}. In these FETs, the empty space, typically air or vacuum, between the recessed gate and the crystal surface forms the gate dielectric. Such devices have the advantage that the gated semiconductor surface is pristine. The transport characteristics of the completed crystal FETs were then measured under vacuum. Subsequently, doping of the same crystals was accomplished by exposing the FETs to the N-silane vapour using the quartz hot wall apparatus shown schematically in Fig. 1a. Contact of the

¹Department of Chemical Engineering and Materials Science, University of Minnesota, Minneapolis, MN, USA. ²State Key Laboratory of Crystal Materials, Shandong University, Jinan, Shandong, China. ³Universität Würzburg, Institut für Organische Chemie & Center for Nanosystems Chemistry, Am Hubland, Würzburg, Germany. ⁴Department of Chemistry, University of Minnesota, Minneapolis, MN, USA. ⁵Department of Electrical and Computer Engineering, University of Minnesota, Minneapolis, MN, USA. [™]e-mail: the@sdu.edu.cn; frisbie@umn.edu

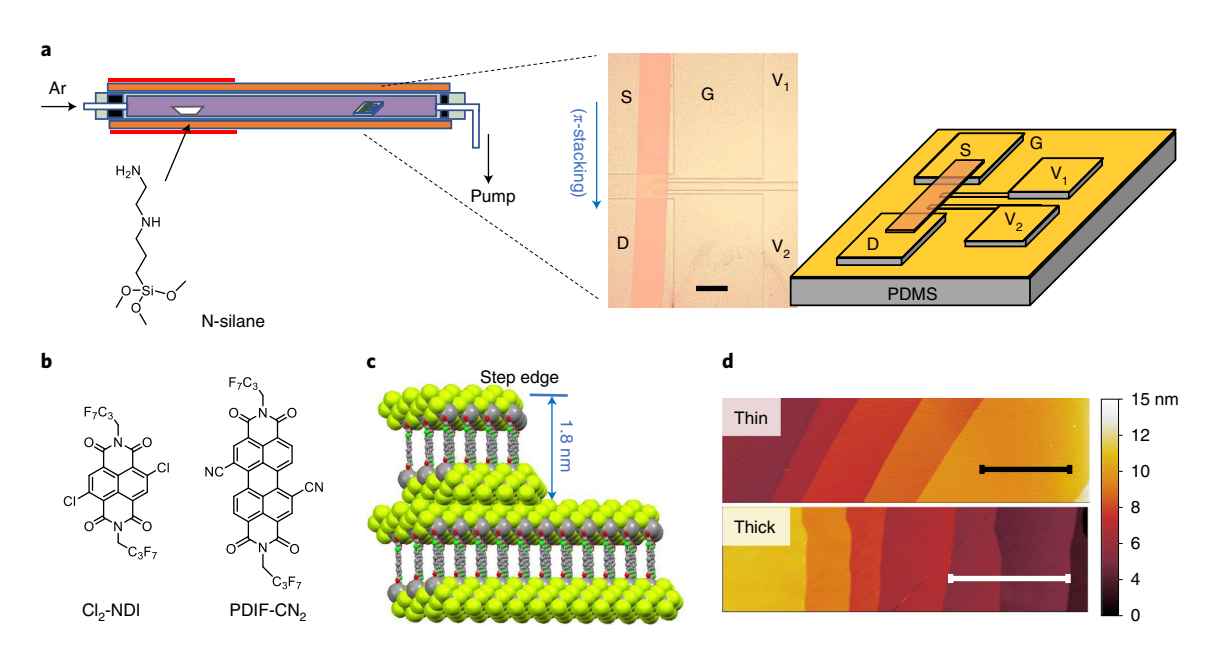


Fig. 1 | Chemical doping of Cl_2 -NDI and PDIF-CN₂ single crystals by exposure to N-silane vapour. **a**, Schematic diagram of the set-up for chemical doping as well as an optical micrograph and scheme of a four-terminal vacuum-gap FET on Au-coated PDMS. The chemical structure of the N-silane dopant is shown. S, D and G represent the FET source, drain and gate electrodes, respectively. V_1 and V_2 are two voltage sensing channel electrodes. Scale bar, 300 μm. **b**, Molecular structures of Cl_2 -NDI and PDIF-CN₂. **c**, Side view of the crystal packing in the 1.8-nm-thick (001) planes of Cl_2 -NDI. A step edge is depicted showing how the pi-system of the Cl_2 -NDI molecules at the edge is exposed. The peripheral fluoroalkyl chains of the Cl_2 -NDI molecules are drawn in a space-filling format. Pi-stacking of the Cl_2 -NDI aromatic cores facilitates electron transport within the (001) planes. The red, green, blue, grey, white and yellow-coloured atoms represent O, Cl, N, C, H and F, respectively. PDIF-CN₂ has a similar packing structure but a different molecular tilt angle within the (001) planes. **d**, AFM topography images of the step density for Cl_2 -NDI single crystals with crystal thicknesses of 3 μm (top) and 40 μm (bottom), respectively. Note the difference in the scale bars (thin, 10 μm, and thick, 1 μm).

N-silane vapour with the crystal face forming the FET channel was possible because of the air-gap FET design.

Figure 2a shows representative FET drain current versus gate voltage (I_D-V_G) characteristics for a relatively thick (47 µm) Cl₂-NDI crystal before and after exposure to 100 µl of N-silane (for all FET results the source is grounded, $V_s = 0$). The undoped, as-grown crystal exhibits n-type field-effect conduction as expected (turning ON as V_G becomes more positive), and after exposure to the N-silane there is a clear negative shift in the onset voltage, as well as improvement of the maximum conductance in the ON state. Note for example that at $V_G = 0 \text{ V}$, I_D is five orders of magnitude greater after doping. The drain current-drain voltage (I_D-V_D) characteristics also reveal substantial differences, Fig. 2b. After doping, the crystal does not show characteristic current saturation, and the currents at the same V_G and V_D values are more than an order of magnitude higher than for the same crystal before doping. The transport results in Fig. 2a,b clearly indicate n-type doping for the thick Cl₂-NDI crystal. However, thin (2.9 μm) Cl₂-NDI crystal results are much different (Supplementary Fig. 6). Exposure of thin crystals to the N-silane does not produce a large onset voltage shift, nor does it result in any notable change in maximum ON current. There is only a change in the OFF current at negative $V_{\rm G}$ values. The results in Fig. 2a and Supplementary Fig. 6 are representative of many experiments on thick and thin crystals. Evidently, crystal thickness somehow plays a vital role in the doping effect. We carried out the same doping experiments with PDIF-CN₂ crystals and found essentially the same results (Supplementary Fig. 7).

We have shown previously that the crystallographic step-edge density on the (001) surface of as-grown Cl₂-NDI and PDIF-CN₂ crystals is highly correlated with crystal thickness²³; others have shown similar results for rubrene crystals³². Furthermore, we have demonstrated that the step edges (Fig. 1c) serve as electron traps in

FET measurements on Cl₂-NDI and PDIF-CN₂ crystals²³. It therefore seemed reasonable that the doping effects were actually directly related to step density, rather than crystal thickness. Figure 1d shows atomic force microscopy (AFM) images of one-unit-cell-tall steps on both the thick and thin crystals of Cl2-NDI (note the difference in scale bars). Figure 2c displays ON-state sheet conductance $\sigma_{\rm s}$ at $V_{\rm G}$ = +60 V for a large number of as-grown (93) and doped (64) Cl₂-NDI and PDIF-CN₂ crystals as a function of step density. For as-grown Cl₂-NDI and PDI-CN₂ crystals, σ_s decreases strongly with step density. However, the dependence is opposite for doped crystals. For doped crystals, σ_s increases with step density. These trends do not reflect changes in contact resistance on doping as the contact resistance in these devices is small relative to the channel resistance (Supplementary Fig. 8). The FET threshold voltages $V_{\rm T}$ shown in Fig. 2d also trend oppositely for as-grown versus doped samples. For as-grown crystals, V_T becomes more positive with increasing step density, consistent with step-edge trapping that we have reported previously²³. For doped crystals, V_T is increasingly negative as step density increases, that is, turning the FET channel OFF requires strongly negative gate voltages, consistent with increased n-doping as step density increases. The data in Fig. 2c,d are indeed consistent with the critical role of step edges in the doping mechanism. Definitive resolution as to whether crystal thickness or surface step-edge density is the key factor in the doping mechanism—as the two structural characteristics are proportional to each other—is presented below, but first we complete the discussion of transport effects.

The temperature dependences of the FET $I_{\rm D}$ – $V_{\rm G}$ characteristics for the same Cl₂-NDI crystal in its as-grown and doped states, respectively, are shown in Fig. 3a,b. The linear regime electron mobility (μ) and threshold voltages extracted from these traces are displayed in Fig. 3c,d (see also Supplementary Fig. 9 for $V_{\rm G}$ dependence

NATURE MATERIALS ARTICLES

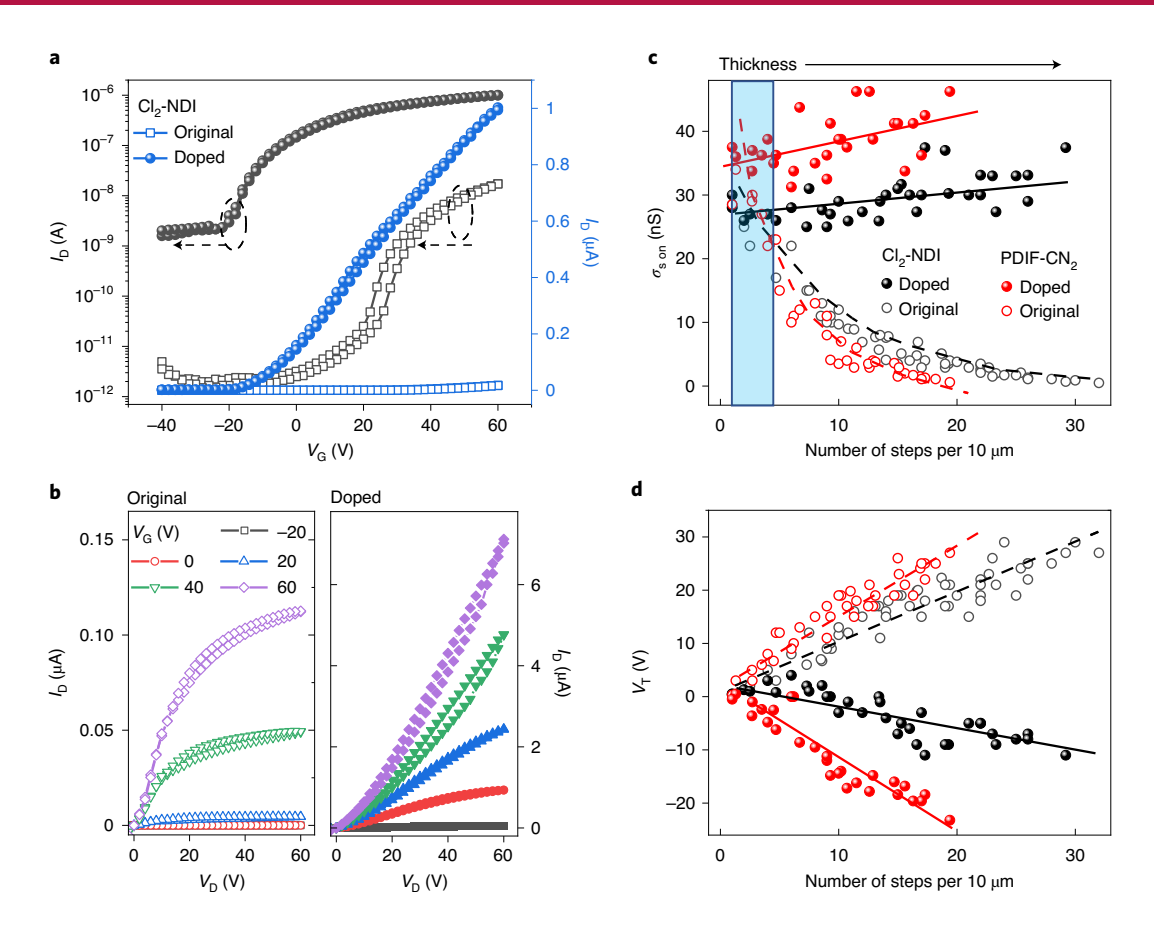
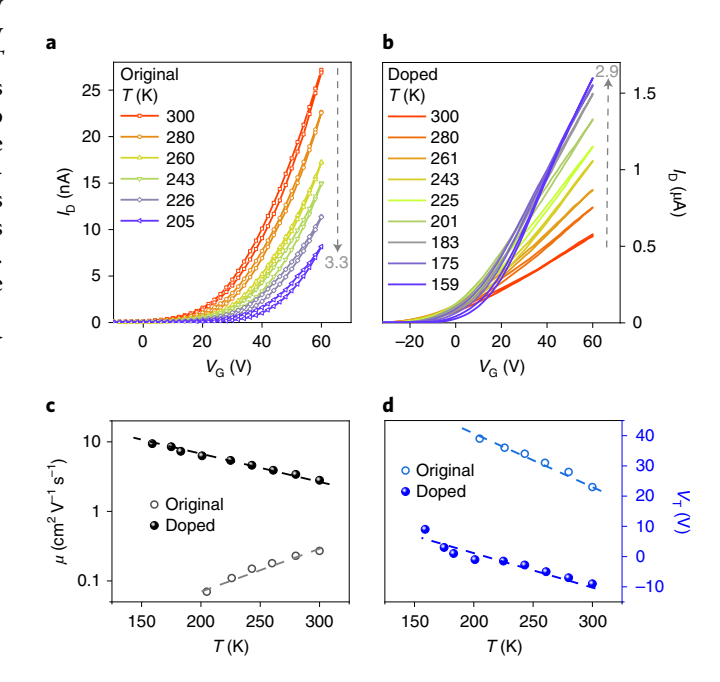


Fig. 2 | Impact of doping on n-type single crystal FET characteristics. **a**, FET I_D – V_G characteristics for a thick (47 μm) Cl₂–NDI crystal with high step density before (open squares) and after (solid circles) exposure to N-silane vapour (100 μl for 1 h, Methods). V_D = 10 V. The thickness and step density of the single crystal are 47 μm and 29 steps per 10 μm, respectively. **b**, Corresponding I_D – V_D characteristics for the same single crystal FET before (left) and after (right) doping. **c,d**, Doping effect on σ_s (**c**) and V_T (**d**) as a function of crystal step density for scores of Cl₂–NDI (black) and PDIF-CN₂ (red) crystals. σ_s is extracted at fixed V_G = 60 V and V_D = 10 V. The narrow light blue stripe in **c** highlights thin crystals with band-like charge transport.

of mobility). The doped crystal exhibits a factor of ten higher room temperature electron mobility and the mobility increases as temperature decreases, reaching $9.4\,\mathrm{cm^2\,V^{-1}s^{-1}}$ at $150\,\mathrm{K}$, which is indicative of band-like transport. For the as-grown crystal the mobility is significantly lower at all temperatures and clearly thermally activated, consistent with trapping. The profoundly different $\mu\text{--}T$ behaviour in Fig. 3c suggests substantial reduction of shallow traps on the surface of the doped crystal $^{33-35}$. The V_{T} behaviour is also consistent with this interpretation. For the doped crystal, the slope of the V_{T} -T correlation is two to three times smaller than the corresponding slope for the same crystal in its as-grown state, and V_{T} is only a few volts even at $150\,\mathrm{K}$ for the doped version, whereas it is tens of volts for the as-grown case (Fig. 3d and Supplementary Fig. 10). The smaller V_{T} values and the weaker temperature dependence

Fig. 3 | Impact of doping on the temperature dependence of electron transport. a,b, Temperature-dependent $I_{\rm D}$ – $V_{\rm G}$ characteristics ($V_{\rm D}$ =10 V) for an individual thick Cl₂–NDI crystal FET before (**a**) and after (**b**) doping. The vertical dashed arrows indicate the trends in $I_{\rm D}$ with decreasing temperature and the numbers at the arrowheads indicate that $I_{\rm D}$ exhibits a 3.3-fold decrease and a 2.9-fold increase, respectively, for original and doped devices on cooling. **c,d**, Corresponding behaviour of μ (**c**) and $V_{\rm T}$ (**d**) versus temperature. The dashed lines are guides to the eye. Channel dimensions are L = 300 μm and W = 490 μm. The step density is around 25 steps per 10 μm. Mobility is extracted from linear fits to the $I_{\rm D}$ – $V_{\rm G}$ characteristic at $V_{\rm G}$ = 60 V.

are consistent with less trapping for the doped crystal^{36,37}. Together, the μ and $V_{\rm T}$ behaviours thus reveal a strong qualitative improvement in the transport behaviour for Cl₂-NDI crystals on doping.



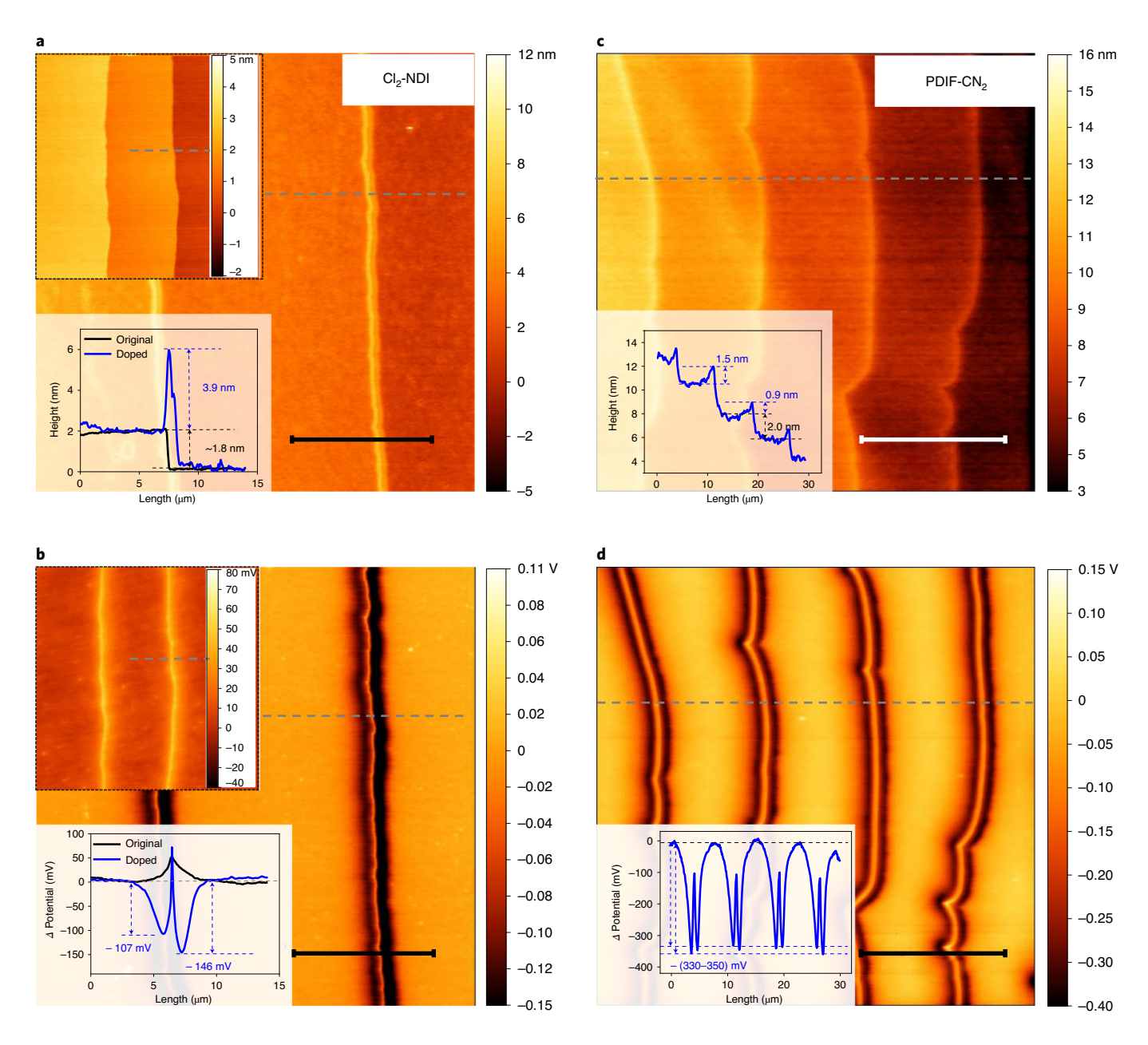


Fig. 4 | AFM height and SKPM potential images of doped crystals. a,b, AFM topography (**a**) and SKPM potential (**b**) images of a doped Cl₂-NDI single crystal. Inset to **a** shows the AFM height image of the original crystal and the comparison of height profiles before and after doping along the grey dashed lines. Inset to **b** shows the potential image of the original crystal and the comparison of potential profiles before and after doping, along the grey dashed lines. **c,d**, AFM topography (**c**) and SKPM potential (**d**) images of a doped PDIF-CN₂ single crystal. Insets to **c** and **d** show the corresponding height and potential profiles along the grey dashed lines, respectively. Scale bars, 10 μm.

Again, similar observations were made for as-grown and doped PDIF- CN_2 crystals (Supplementary Fig. 11). Furthermore, pronounced band-like charge transport was observed in all doped devices, regardless of thickness or step density, which was in sharp contrast to the as-grown crystals that displayed band-like behaviour only for the very thinnest crystals, that is, those with the lowest step densities (Fig. 2c). We note also that the doped devices were stable. Mobilities for devices stored in air for two months degraded by only about 18% (Supplementary Figs. 12 and 13).

We turn now to the mechanism of n-doping. The size of the N-silane molecule and the tight-packing of the $\text{Cl}_2\text{-NDI}$ and PDIF- CN_2 crystals suggested to us that the doping mechanism was a surface, not a bulk, phenomenon, as has been reported

before for fluoroalkyl silane surface doping of rubrene crystals ^{16,38}. To prove this point we carried out depth profiling experiments to measure the concentration of N-silane as a function of depth into the crystal. The data indicate that indeed the N-silane does not penetrate into the bulk of the crystal, but is confined to the surface, as expected (Supplementary Fig. 14). Additionally, X-ray diffraction revealed no evidence of crystal expansion after doping (Supplementary Fig. 15)^{18,39}.

To understand the surface effects of N-silane exposure, we undertook scanning probe microscopy analysis of the crystal surfaces. Figure 4a,c shows the topographic AFM images of the Cl₂-NDI and PDIF-CN₂ surfaces after N-silane doping. A clear ridge, several nanometres high, is evident at each step edge. Such ridges are

NATURE MATERIALS ARTICLES

not evident in untreated crystals, indicating the N-silane selectively interacts with molecules at the step edges (see another example in Supplementary Fig. 16). As noted already, N-silane readily undergoes electron transfer reactions with Cl2-NDI and PDIF-CN2 in solution to make the corresponding radical anions (Supplementary Fig. 4, 5). This is illustrated for the case of Cl₂-NDI in Fig. 5a, which shows the UV-vis absorption spectra for Cl₂-NDI on spectroelectrochemical reduction in solution in comparison to the observations for a thin film of Cl₂-NDI exposed to N-silane. The bands at roughly 480, 520 and 600 nm are clear signatures of the Cl₂-NDI radical anion (Supplementary Fig. 4)40. Similar results are obtained for PDIF-CN₂ in solution (Supplementary Fig. 5). For the crystals, we speculate that N-silane can reduce Cl₂-NDI and PDIF-CN₂ molecules located at the step edges because the redox-active pi-cores of the molecules are exposed on the step faces (Fig. 1c). In contrast, the crystalline terraces, which correspond to the (001) planes, are terminated with fluoroalkyl chains that effectively block molecular interaction and electron transfer. Thus, it is the unit cell structure of Cl₂-NDI and PDIF-CN₂ crystals, combined perhaps with the less aggressive reducing power of the N-silane, which provides the step-edge specificity of the doping chemistry. Silanes are known to undergo oligomerization, and once reaction has occurred at the step edge further reactions may follow to create a several-nanometre thick N-silane multilayer stripe as shown in Fig. 4a,c (ref. 41).

The SKPM images in Fig. 4b,d, which correspond to the topographic images in Fig. 4a,c, show striking electric potential contrast^{38,42}. Coincident with each step edge for both doped crystals, positive and negative potential stripes are clearly evident. In particular, one sees that the positive stripe at each step edge is flanked by negative potential stripes on either side. Insets to the panels show line scans across the step-edge potential stripes. From the profile in Fig. 4b for Cl₂-NDI, it is evident that the peak positive potential is roughly $+50 \,\mathrm{mV}$ and the peak negative potential exceeds $-100 \,\mathrm{mV}$, which are both very large values. The total width of the entire stripe is nearly 5 µm. For PDIF-CN₂ in Fig. 4d, the results are similar, with the exception that the peak negative potentials are even lower, that is, less than -300 mV. In our previous work on undoped crystals, only positive SKPM potentials were observed at step edges²³. Thus, the potential signatures measured at the step edges have completely changed after treatment with the N-silane. To assess the robustness of the Fig. 4 results, we have carried out many SKPM experiments under different scanning conditions and modes (for example, amplitude modulation versus frequency modulation). While the precise potentials observed in Fig. 4 depend on tip lift height and a.c. bias, the overall 'triple stripe' pattern at the step edges is always observed for doped crystals, and it is distinct from the step-edge potential measured for undoped samples (Supplementary Figs. 16–30).

We also undertook UV photoelectron spectroscopy (UPS) measurements of doped crystals with high step densities to confirm our interpretation of the effects of N-silane exposure. UPS is a classical technique for examining band alignment in doped semiconductors⁴³⁻⁴⁶ and in this case, it also has the advantage that it averages over a geometrical area much larger than the distances between steps and so provides complementary information to SKPM. Figure 5b compares the UPS results for doped and as-grown Cl₂-NDI crystals in the valence (highest occupied molecular orbital, HOMO) band and photoelectron cut-off regions (Supplementary Fig. 31). It is clear that the surface-doped Cl₂-NDI crystals display both a 0.3 eV deeper HOMO and a 0.5 eV smaller work function (higher binding energy at cut-off). These results are depicted in the energy level diagram on the right side of Fig. 5b. Positive ionization of the N-silane by electron donation to subsurface layers of the crystal results in an effective dipole at the crystal surface that lowers the work function (that is, it creates a downward vacuum level shift), consistent with the UPS observation. Likewise, a higher HOMO binding energy relative to the Fermi level for the doped crystal is

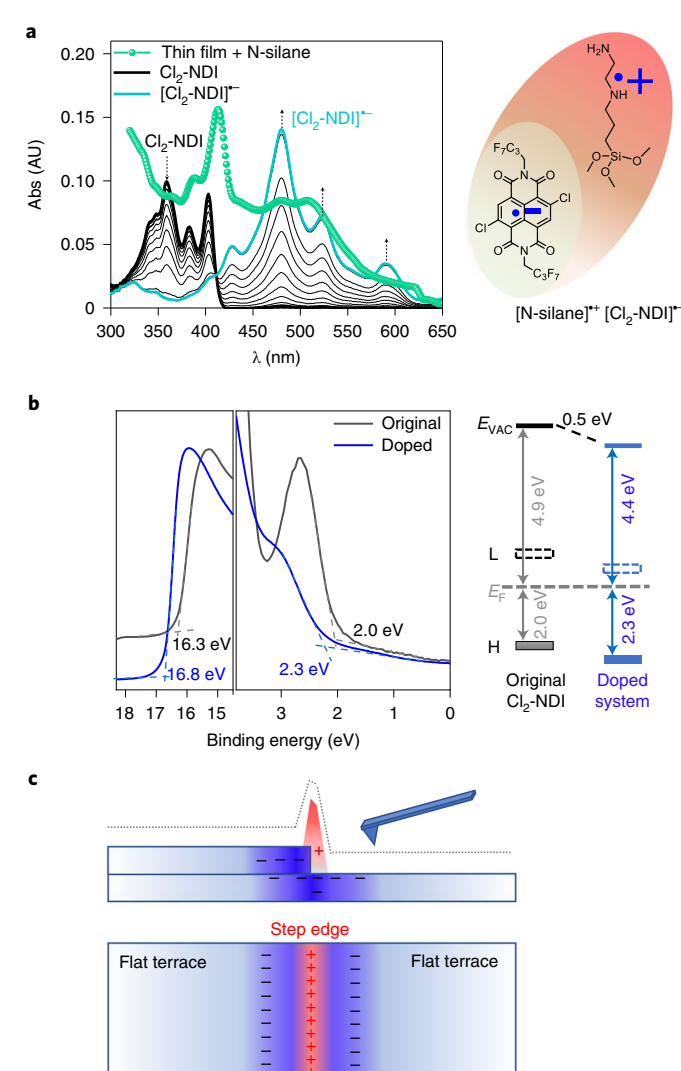


Fig. 5 | Spectroscopic evidence for doping and scheme of the dopant-induced space charge distribution. a, UV-vis absorption spectra for a thin film of Cl₂-NDI exposed to N-silane in comparison to the spectroelectrochemical reduction of Cl₂-NDI in CHCl₃ solution to the [Cl₂-NDI] - radical anion. **b**, UPS measurement of a Cl₂-NDI single crystal (with a very high step density) before and after doping (left), and corresponding energy level line-up for the pristine and n-doped systems (right). The doped crystal has a smaller work function because of the positive ionization of surface-confined donors; the increased HOMO-to- E_F offset is consistent with n-type doping. H, HOMO; L, LUMO; E_{VAC} , vacuum energy. **c**, Scheme of the space charge distribution across a crystal step edge due to positively ionized donors and the associated electron atmosphere. The upper image shows schematic side-views of the step-edge topography and the charge distribution. Lower image is the corresponding plan-view of the charge distribution indicating a line of positively ionized donors (red area) and the associated negatively charged electron atmosphere (dark blue area). The + and - symbols and the red and blue shading, respectively, denote the sign and distribution of charge; electroneutrality requires that positive and negative charges balance, which is not shown explicitly.

indicative of a downward shift in the LUMO (lowest unoccupied molecular orbital) and HOMO energies and thus indeed reflects n-doping (the LUMO-to-Fermi level offset is reduced). Thus, the UPS data in Fig. 5b are consistent with the n-type step-edge doping mechanism.

From our collective experiments, an explanation for the potential images in Fig. 4b,d thus emerges; we conclude that ionized donors, localized at the step edges, create a narrow line of positive charge that is then screened by mobile electrons and the crystal dielectric response. The positive and negative charge distributions associated with a single step edge are depicted schematically in Fig. 5c. Narrow bright stripes in Fig. 4b,d correspond to the positive donor line charge; the broader, flanking dark stripes correspond to the negatively charged electron atmospheres confined to the vicinity of the step edges by the Coulomb potential of the ionized donors. It is this triple stripe space charge distribution at each step edge that is captured by the SKPM potential images, providing a striking visualization of microscopic charge transfer effects in organic semiconductors. Indeed, SKPM has well-known sensitivity to charge^{47–51} and, in future work, computational simulation of both the charge distribution and full tip-sample interaction will be used to quantitatively relate the unusual shapes of the measured potentials to the charge density profiles⁴⁷. For the present, we note simply that the shapes and spatial extents of the potentials definitively reflect doping-induced electron distributions in the vicinity of positive surface line charges.

In conclusion, we have discovered a site-specific n-type doping mechanism on the surfaces of single crystals of two benchmark organic semiconductors. The site-specific doping simultaneously eliminates electron traps and increases the background electron concentration, which in turn leads to superior ON-state conductances for FETs based on the doped crystals. The doping mechanism targets specific, well-defined structural features on the surfaces of the crystals—namely, step edges—that have been shown to be detrimental to transport. This site-specific trap elimination and doping in crystalline organic semiconductors offers the intriguing possibility of a general strategy in which targeted doping chemistry selectively 'erases' the effects of well-defined trap states. A general strategy of course hinges on continued identification of other well-defined structural features, such as grain boundaries, which serve as charge traps in crystalline organic materials, and specific doping chemistry that can address them.

Our study has also provided salient images of doping-induced space charge in organic semiconductor crystals. In the context of organic semiconductor science, this is gratifying confirmation that the classical picture of doping in conventional semiconductors applies well to organic systems. Specifically, the SKPM images demonstrate that electrons released into the host crystal by ionized donors are mobile and delocalize subject to the Coulomb potential associated with the spatially localized ionized donors along the step edges. We anticipate that site-specific chemical doping demonstrated here, in combination with SKPM imaging, will be a powerful approach for further understanding of microscopic doping effects and defects in crystalline organic semiconductor systems.

Online content

Any methods, additional references, Nature Research reporting summaries, source data, extended data, supplementary information, acknowledgements, peer review information; details of author contributions and competing interests; and statements of data and code availability are available at https://doi.org/10.1038/s41563-021-01079-z.

Received: 25 April 2020; Accepted: 14 July 2021; Published online: 30 August 2021

References

- Walzer, K., Maennig, B., Pfeiffer, M. & Leo, K. Highly efficient organic devices based on electrically doped transport layers. *Chem. Rev.* 107, 1233–1271 (2007).
- Lussem, B. et al. Doped organic transistors. Chem. Rev. 116, 13714–13751 (2016).

- Xu, Y. et al. Doping: a key enabler for organic transistors. Adv. Mater. 30, 1801830 (2018).
- Kang, K. et al. 2D coherent charge transport in highly ordered conducting polymers doped by solid state diffusion. *Nat. Mater.* 15, 896–902 (2016).
- Lin, X. et al. Beating the thermodynamic limit with photo-activation of n-doping in organic semiconductors. Nat. Mater. 16, 1209–1215 (2017).
- Yamashita, Y. et al. Efficient molecular doping of polymeric semiconductors driven by anion exchange. Nature 572, 634–638 (2019).
- Bolto, B. A., McNeill, R. & Weiss, D. E. Electronic conduction in polymers. III. Electronic properties of polypyrrole. Aust. J. Chem. 16, 1090–1103 (1963).
- Shirakawa, H., Louis, E. J., MacDiarmid, A. G., Chiang, C. K. & Heeger, A. J. Synthesis of electrically conducting organic polymers: halogen derivatives of polyacetylene, (CH), J. Chem. Soc. Chem. Commun. 16, 578–580 (1977).
- Baughman, R. H., Bredas, J. L., Chance, R. R., Elsenbaumer, R. L. & Shacklette, L. W. Structural basis for semiconducting and metallic polymer dopant systems. *Chem. Rev.* 82, 209–222 (1982).
- Garito, A. F. & Heeger, A. J. Design and synthesis of organic metals. Acc. Chem. Res. 7, 232–240 (1974).
- Chiang, C. K. et al. Electrical conductivity in doped polyacetylene. *Phys. Rev. Lett.* 39, 1098–1101 (1977).
- Ferraris, J., Cowan, D. O., Walatka, V. & Perlstein, J. H. Electron transfer in a new highly conducting donor-acceptor complex. J. Am. Chem. Soc. 95, 948–949 (1973).
- Bryce, M. R. Recent progress on conducting organic charge-transfer salts. Chem. Soc. Rev. 20, 355–390 (1991).
- Huang, J. et al. Low-voltage organic electroluminescent devices using pin structures. Appl. Phys. Lett. 80, 139–141 (2002).
- Zhou, X. et al. Very-low-operating-voltage organic light-emitting diodes using a p-doped amorphous hole injection layer. *Appl. Phys. Lett.* 78, 410-412 (2001).
- Calhoun, M. F., Sanchez, J., Olaya, D., Gershenson, M. E. & Podzorov, V. Electronic functionalization of the surface of organic semiconductors with self-assembled monolayers. *Nat. Mater.* 7, 84–89 (2008).
- Alves, H., Molinari, A. S., Xie, H. & Morpurgo, A. F. Metallic conduction at organic charge-transfer interfaces. *Nat. Mater.* 7, 574–580 (2008).
- Duong, D. T., Wang, C., Antono, E., Toney, M. F. & Salleo, A. The chemical and structural origin of efficient p-type doping in P₃HT. Org. Electron. 14, 1330–1336 (2013).
- Han, Y. et al. Anion-induced N-doping of naphthalenediimide polymer semiconductor in organic thin-film transistors. npj Flex. Electron. 2, 11 (2018).
- Lu, G. et al. Moderate doping leads to high performance of semiconductor/ insulator polymer blend transistors. Nat. Commun. 4, 1588 (2013).
- Olthof, S. et al. Ultralow doping in organic semiconductors: evidence of trap filling. *Phys. Rev. Lett.* 109, 176601 (2012).
- He, T. et al. Single-crystal field-effect transistors of new Cl₂-NDI polymorph processed by sublimation in air. Nat. Commun. 6, 5954 (2015).
- He, T. et al. Crystal step edges can trap electrons on the surfaces of n-type organic semiconductors. Nat. Commun. 9, 2141 (2018).
- Jones, B. A. et al. High-mobility air-stable n-type semiconductors with processing versatility: dicyanoperylene-3,4:9,10-bis(dicarboximides). Angew. Chem. Int. Ed. 43, 6363–6366 (2004).
- Minder, N. A., Ono, S., Chen, Z., Facchetti, A. & Morpurgo, A. F. Band-like electron transport in organic transistors and implication of the molecular structure for performance optimization. *Adv. Mater.* 24, 503–508 (2012).
- Russ, B. et al. Tethered tertiary amines as solid-state n-type dopants for solution-processable organic semiconductors. Chem. Sci. 7, 1914–1919 (2016).
- Park, J. et al. Single-gate bandgap opening of bilayer graphene by dual molecular doping. Adv. Mater. 24, 407–411 (2012).
- Lee, B. H., Bazan, G. C. & Heeger, A. J. Doping-induced carrier density modulation in polymer field-effect transistors. Adv. Mater. 28, 57–62 (2016).
- Röger, C. & Würthner, F. Core-tetrasubstituted naphthalene diimides: synthesis, optical properties, and redox characteristics. *J. Org. Chem.* 72, 8070–8075 (2007).
- Kishore, R. S. K. et al. Ordered and oriented supramolecular n/p-heterojunction surface architectures: completion of the primary color collection. J. Am. Chem. Soc. 131, 11106–11116 (2009).
- Sundar, V. C. et al. Elastomeric transistor stamps: reversible probing of charge transport in organic crystals. Science 303, 1644–1646 (2004).
- Kim, J. J. et al. Correlating crystal thickness, surface morphology, and charge transport in pristine and doped rubrene single crystals. ACS Appl. Mater. Interfaces 10, 26745–26751 (2018).
- Materials, D. et al. Simulation of temperature-dependent charge transport in organic semiconductors with various degrees of disorder. *J. Chem. Theory Comput.* 12, 3087–3096 (2016).
- Podzorov, V. et al. Intrinsic charge transport on the surface of organic semiconductors. *Phys. Rev. Lett.* 93, 086602 (2004).
- 35. Mei, Y. et al. Crossover from band-like to thermally activated charge transport in organic transistors due to strain-induced traps. *Proc. Natl Acad. Sci. USA* 114, 6739–E6748 (2017).

NATURE MATERIALS ARTICLES

- Xie, H., Alves, H. & Morpurgo, A. F. Quantitative analysis of density-dependent transport in tetramethyltetraselenafulvalene single-crystal transistors: intrinsic properties and trapping. *Phys. Rev. B.* 80, 245305 (2009).
- 37. Zuo, G. et al. Molecular doping and trap filling in organic semiconductor host–guest systems. *J. Phys. Chem. C.* **121**, 7767–7775 (2017).
- Ellison, D. J., Lee, B., Podzorov, V. & Frisbie, C. D. Surface potential mapping of SAM-functionalized organic semiconductors by Kelvin probe force microscopy. Adv. Mater. 23, 502–507 (2011).
- Kleemann, H. et al. Structural phase transition in pentacene caused by molecular doping and its effect on charge carrier mobility. Org. Electron. 13, 58–65 (2012).
- Guha, S., Goodson, F. S., Corson, L. J. & Saha, S. Boundaries of anion/ naphthalenediimide interactions: from anion-π interactions to anion-induced charge-transfer and electron-transfer phenomena. *J. Am. Chem. Soc.* 134, 13679–13691 (2012).
- Chauhan, A. K. et al. Self-assembly of the 3-aminopropyltrimethoxysilane multilayers on Si and hysteretic current-voltage characteristics. *Appl. Phys. A* 90, 581–589 (2007).
- Tello, M., Chiesa, M., Duffy, C. M. & Sirringhaus, H. Charge trapping in intergrain regions of pentacene thin film transistors. *Adv. Funct. Mater.* 18, 3907–3913 (2008).
- 43. Winkler, S. et al. Probing the energy levels in hole-doped molecular semiconductors. *Mater. Horiz.* **2**, 427–433 (2015).

- 44. Lussem, B. et al. Doped organic transistors operating in the inversion and depletion regime. *Nat. Commun.* 4, 2775 (2013).
- Mendez, H. et al. Charge-transfer crystallites as molecular electrical dopants. Nat. Commun. 6, 8560 (2015).
- Salzmann, I. et al. Intermolecular hybridization governs molecular electrical doping. Phys. Rev. Lett. 108, 035502 (2012).
- 47. Sadewasser S. & Glatzel, S. Kelvin Probe Force Microscopy: From Single Charge Detection to Device Characterization (Springer, 2018).
- Somoza, A. M. & Palacios-Lidón, E. Localized charges in thin films by Kelvin probe force microscopy: from single to multiple charges. *Phys. Rev. B.* 101, 075432 (2020).
- Turek, N., Godey, S., Deresmes, D. & Mélin, T. Ring charging of a single silicon dangling bond imaged by noncontact atomic force microscopy. *Phys. Rev. B.* 102, 235433 (2020).
- 50. Zhang, Q. et al. Measurement and manipulation of the charge state of an adsorbed oxygen adatom on the rutile $TiO_2(110)-1\times 1$ surface by nc-AFM and KPFM. J. Am. Chem. Soc. **140**, 15668–15674 (2018).
- Adachi, Y. et al. Elucidating the charge state of an Au nanocluster on the oxidized/reduced rutile TiO₂ (110) surface using non-contact atomic force microscopy and Kelvin probe force microscopy. *Nanoscale Adv.* 2, 2371–2375 (2020).

Publisher's note Springer Nature remains neutral with regard to jurisdictional claims in published maps and institutional affiliations.

© The Author(s), under exclusive licence to Springer Nature Limited 2021

Methods

Materials. Cl₂-NDI was synthesized according to the literature⁵². PDIF-CN₂ is commercially available from Flexterra Inc. (Polyera Activink N1100). All dopants were purchased from Sigma-Aldrich.

Four-terminal FET fabrication. As described previously, high-quality single crystals were grown by the physical vapour transport method and then laminated onto a prepatterned Au-coated PDMS substrate featuring source, drain, gate and channel electrodes to make a four-terminal FET. The crystal long-axis corresponding to the pi-stacking direction was aligned perpendicular to the source and drain electrodes as shown in Fig. 1 (refs. 23,25). All contact electrodes consisted of a Cr (3 nm)/Au (20 nm) bilayer film. The distance between the source and drain electrodes was 300 μm and the distance between the two channel measurement electrodes (V $_1$ and V $_2$) was 150 μm . The gate-to-crystal gap was 5 μm for all devices. The specific capacitance of the crystal-gap-gate stack was 0.18 nF cm 2 . The I-V characteristics of the devices were measured in an N $_2$ -filled glovebox and variable temperature measurements were carried out in the dark with a cryogenic probe station at 10^{-4} Torr.

N-silane doping. To carry out doping, a single crystal FET was removed from the FET probe station and placed in the quartz doping vessel along with a small glass dish containing a well-defined volume of the N-silane liquid (typically 50–300 μl depending on the desired dose). The vessel was closed and evacuated to 0.1 Torr. A small Ar flow was established and then the walls of the vessel were heated resistively. The wall temperature surrounding the dopant dish was increased to 80 °C and the wall temperature of the device end of the vessel was heated to 50 °C. After 1 h, the liquid in the dish was completely evaporated, the N-silane was purged by increasing the Ar gas flow, and the apparatus was cooled. The treated FET was removed and transferred back to the vacuum probe station for electrical measurements.

Molecular characterization. 1 H-nuclear magnetic resonance spectra were recorded with a Bruker $400\,\mathrm{MHz}$ spectrometer. UV-vis absorption spectra were recorded with a Spectronic Genesys spectrometer in transmission mode. Spectra of the radical anions were recorded in reflection mode using a three-electrode custom-made electrochemical cell inserted in an Agilent Cary $5000\,\mathrm{UV-vis}$ near infrared spectrometer (electrolyte was $0.1\,\mathrm{M}$ Bu $_4\mathrm{NPF}_6$ in dry CHCl $_3$, with a 6-mm-diameter Pt-disc working electrode, Pt counter and Ag/AgCl leak free reference electrode (Warner Instruments)). The optical path was adjusted to $100\,\mathrm{\mu m}$ with a micrometre screw. Potentials were applied with a reference $600\,\mathrm{potentiostat}$ (Gamry Instruments). Application of potential steps and recording of absorption spectra was automated by a Lab View routine.

X-ray diffraction and X-ray photoelectron spectra (XPS)/UPS analysis.

High-resolution X-ray diffraction was carried out with a Philips Panalytical X'Pert Pro diffractometer with monochromatic Cu K α radiation (wavelength 0.154 nm) at tube settings of 45 kV and 40 mA. XPS and UPS were taken on an PHI VersaProbe III (10^-8 Torr) equipped with a hemispherical analyser, using an Al K α X-ray monochromatic source (1,486.6 eV) and He discharge lamp ($h\nu$ (HeI) = 21.22 eV) as excitation sources, respectively. For XPS, the X-ray anode was operated at 200 W, and the analyser was set to a pass energy of 280 eV for survey scans and 112 eV for high-resolution scans. The samples were prepared, stored and transferred under an N_2 atmosphere until introduced to the measurement apparatus.

SKPM. Measurements were performed with a Bruker Instruments Nanoscope V Multimode AFM with conductive probes from Mikromasch USA (NSC18,

Pt coated, resonant frequency 60–90 kHz, $k=2-5.5\,\mathrm{N\,m^{-1}}$, $R_\mathrm{C}=25\,\mathrm{nm}$). SKPM topography and potential scans were conducted with a tip d.c. voltage $V_\mathrm{AC}=6\,\mathrm{V}$ and lift height $d=10\,\mathrm{nm}$ inside an Ar-filled glovebox with oxygen levels (roughly 1 ppm) to mitigate surface contamination effects. Other scanning conditions and corresponding images are given in the Supplementary Information.

Data availability

The experimental data that support the findings of this study are available online at $\frac{1}{1000}$ https://doi.org/10.6084/m9.figshare.13602551.

References

 Oh, J. H. et al. High-performance air-stable n-type organic transistors based on core-chlorinated naphthalene tetracarboxylic diimides. *Adv. Funct. Mater.* 20, 2148–2156 (2010).

Acknowledgements

This work was supported primarily by the MRSEC programme of the National Science Foundation (NSF) under grant no. DMR-2011401 (T.H.). C.D.F. also acknowledges partial support from grant no. NSF DMR-1806419 and the University of Minnesota (P.P.R. and Y.W.). Parts of this work were carried out in the College of Science and Engineering Characterization Facility, University of Minnesota, which has received capital equipment funding from the NSF through the UMN MRSEC programme under award no. DMR-2011401, and in the Minnesota Nano Center, which is supported by NSF through the National Nano Coordinated Infrastructure Network, under award no. ECCS-2025124. Parts of this work were also carried out at the Center for Nanosystems Chemistry at the Universität Würzburg, which has received funds from the Bavarian State Ministry of Science and Arts in the framework of the research programme 'Solar Technologies Go Hybrid' (F.W.). Some of the SKPM measurements were performed at Shandong University, supported by the National Natural Science Foundation of China grant no. 62074093 (T.H.). T.H. also acknowledges support from the Qilu Young Scholars Programme of Shandong University.

Author contributions

C.D.F. designed and guided the research programme. T.H. grew single crystals, fabricated the devices and performed measurements and analysis. M.S., R.R. and F.W. synthesized the $\mathrm{Cl_2}$ -NDI materials, performed UV-vis near infrared spectroelectrochemistry and contributed to the scientific discussion of the results. P.P.R. and Y.W. provided theoretical support and contributed to the interpretation of the results. T.H. and C.D.F. wrote the paper with input from all authors.

Competing interests

The authors declare no competing interests.

Additional information

Supplementary information The online version contains supplementary material available at https://doi.org/10.1038/s41563-021-01079-z.

Correspondence and requests for materials should be addressed to T.H. or C.D.E.

Peer review information *Nature Materials* thanks Sasha Sadewasser and the other, anonymous, reviewer(s) for their contribution to the peer review of this work.

Reprints and permissions information is available at www.nature.com/reprints.